Optics Letters

Surface Brillouin scattering in photonic crystal fibers

Joël Cabrel Tchahame,[1] Jean-Charles Beugnot,[1] Kien Phan Huy,[1] Vincent Laude,[1]
Alexandre Kudlinski,[2] and Thibaut Sylvestre[1,*]

[1]Institut FEMTO-ST, UMR 6174 CNRS, Université Bourgogne Franche-Comté, 25030 Besançon, France
[2]Laboratoire PhLAM, IRCICA, UMR 8523 CNRS, Université de Lille 1, 59655 Villeneuve D'Asq, France
*Corresponding author: thibaut.sylvestre@univ-fcomte.fr

Received 20 May 2016; accepted 7 June 2016; posted 14 June 2016 (Doc. ID 266731); published 12 July 2016

We report, to the best of our knowledge, the first experimental observation of surface Brillouin scattering in silica-based photonic crystal fibers, arising from the interaction between guided light and surface acoustic waves. This was achieved using small-core and high air-filling fraction microstructured fibers that enable a strong opto-acoustic coupling near the air holes while mitigating the acoustic leakages in the microstructured cladding. It is further shown that this new type of light scattering is highly sensitive to the fiber air-hole microstructure, thus providing a passive and efficient way to control it. Our observations are confirmed through numerical simulations of the elastodynamics equation. © 2016 Optical Society of America

OCIS codes: (060.5295) Photonic crystal fibers; (190.4370) Nonlinear optics, fibers; (290.5830) Scattering, Brillouin.

http://dx.doi.org/10.1364/OL.41.003269

Surface Brillouin scattering is generally referred to as the inelastic scattering of light by surface acoustic waves (SAWs). Known since the 1970s, this effect has widely been used as a contactless measurement technique to investigate elastic properties of thin films, interfaces, and layered opaque materials [1,2]. Unlike Brillouin scattering from bulk acoustic waves, surface Brillouin scattering arises from a small ripple mechanism at the surface of samples. The phonons present at the surface move in thermal equilibrium with very small amplitudes creating corrugation of the surface, which can diffract incident light. Interestingly, although it was primarily demonstrated at the surface of opaque materials, Brillouin scattering from SAWs has also recently been observed in silica-based tapered optical fibers [3,4]. It has been found in particular that such ultrathin optical fibers enable a strong photon–phonon coupling to give rise to a new, previously unexplored regime of Brillouin scattering from SAWs that is absent of conventional optical fibers [3,4]. These surface waves are referred to as Rayleigh waves when they reach the surface phase velocity (e.g., for fused silica, $V_S = 3400\ \mathrm{m{\cdot}s^{-1}}$ [5,6]). When propagating along the fiber taper, SAWs create a moving index grating which in turn backscatters the light with a Brillouin frequency shift of about 6 GHz, which is much lower than that in standard single-mode fibers (SMFs, 11 GHz). The main difference, however, between surface Brillouin scattering on opaque planar materials and in optical waveguides is that the Brillouin frequency shift f_B depends on the effective refractive index n_{eff} in the latter case, as $f_B = 2n_{\mathrm{eff}} V_S/\lambda$, with λ the optical wavelength. Furthermore, in highly-confined optical waveguides, SAWs can be enhanced, removed and controlled through the combined effects of electrostriction and radiation pressure [3,4].

In this Letter we demonstrate surface Brillouin scattering in silica-based solid-core photonic crystal fibers (PCFs). Small-core and high air-filling fraction PCFs were specifically used to allow for the achievement of a strong opto-acoustic coupling near the air holes while mitigating the acoustic leakages in the microstructured cladding. Our experimental and numerical results show new scattered photons from surface acoustic phonons with frequency shifts around 6 GHz by pumping the PCF at a wavelength of 1550 nm. Calculated acoustic velocity and numerical simulations, including the variation of air–silica microstructures, are shown to be in good agreement with the observed Brillouin spectra.

Figure 1(a) shows the scanning electron microscopy (SEM) image of the silica PCF cross-section, specifically designed and manufactured to observe SAWs. It has a triangular lattice with a wavelength-scale hexagonal core and a large air-filling fraction of 0.93. The table in Fig. 1(a) summarizes its main opto-geometric parameters, including its core diameter d_c, hole diameter d, pitch Λ, air-filling fraction d/Λ, and fiber length L. Attenuation α of the fiber was experimentally estimated by optical-time domain reflectometry (OTDR). L_{eff} is the effective length, calculated by $L_{\mathrm{eff}} = (1 - e^{-\alpha L})/\alpha$ [7]. The effective mode area A_{eff} of the fundamental LP_{01} optical mode was numerically computed using a finite element method [COMSOL software, see Fig. 2(b)] from the air-hole microstructure shown in Fig. 1(a).

The experimental setup used for Brillouin spectroscopy is shown schematically in Fig. 1(b). It is based on a heterodyne detection in which the backscattered Brillouin Stokes light from the PCF is coherently coupled with the input light to get a beat note in the electrical domain [8]. As input light,

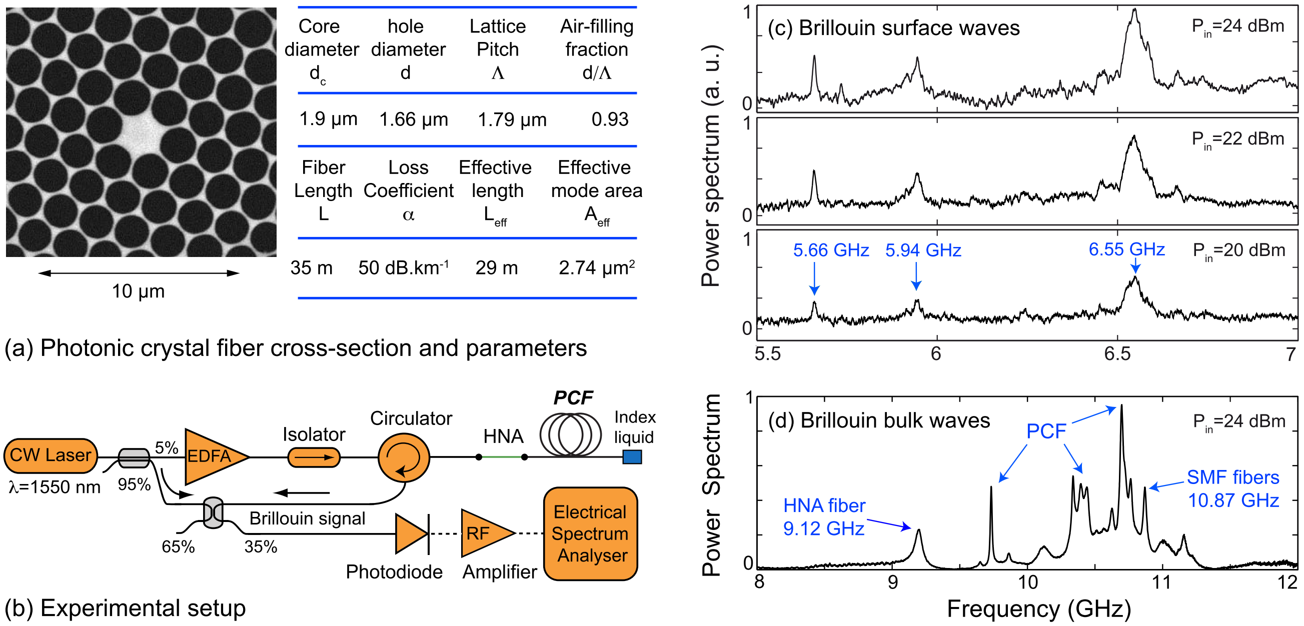

Core diameter d_c	hole diameter d	Lattice Pitch Λ	Air-filling fraction d/Λ
1.9 µm	1.66 µm	1.79 µm	0.93
Fiber Length L	**Loss Coefficient α**	**Effective length L_{eff}**	**Effective mode area A_{eff}**
35 m	50 dB.km^{-1}	29 m	2.74 µm^2

Fig. 1. (a) Cross-section image of the photonic crystal fiber used to investigate surface Brillouin scattering. Right table shows its opto-geometric parameters. (b) Experimental setup for measuring backward Brillouin spectra. (c) Experimental Brillouin spectra for an increasing input power showing the surface acoustic waves around 6 GHz. (d) Experimental Brillouin spectrum showing the bulk acoustic waves around 10 GHz.

we used a continuous and narrow-linewidth (<100 kHz) pump laser running at 1550 nm. It is split into two beams by use of a tap 95/5 fiber coupler. The first 5% beam was amplified by an erbium-doped fiber amplifier (EDFA) and sent to the PCF via an optical circulator. An intermediate high numerical aperture optical fiber (HNA) was spliced in between the single-mode fibers (SMF) and the PCF to get the highest coupling rate. With this technique, the total insertion losses were only 4 dB. The PCF output end was finally immersed in a refractive index-matching liquid to remove detrimental Fresnel reflections. The Brillouin signal coming back from the PCF was coupled to the second pump beam with a second 65/35 fiber coupler. The resulting beat note was detected in the radio-frequency (RF) domain with a fast photodiode (12 GHz bandwidth) and the averaged Brillouin spectra were recorded with an electrical spectrum analyzer (ESA) from 5 GHz to 12 GHz with a resolution of 500 kHz.

Figure 1(c) shows typical Brillouin spectra around 6 GHz for varying input powers from 20 dBm to 24 dBm. Three acoustic resonances are evident at 5.66, 5.94, and 6.55 GHz, respectively. From these Brillouin frequency shifts, we can readily calculate the associated acoustic velocities using the phase-matching condition between the optical and acoustical wavevectors, which reads for a counter-propagating interaction as $\beta_{\mathrm{op}} = 2\beta_{\mathrm{ac}}$ [9]. This yields a phase velocity $V_S = \lambda f_B / 2n_{\mathrm{eff}}$, with f_B the Brillouin frequency shift and $\lambda = 1.55$ µm is the optical wavelength. $n_{\mathrm{eff}} = 1.3622$ is the effective refractive index of the fundamental mode given by numerical simulations [see Fig. 2(b)]. Considering, for instance, the central frequency peak at 5.94 GHz, this gives us a phase velocity of 3380 m·s^{-1} in excellent agreement with the surface phase velocity of silica glass plates [5]. We note that this speed is typical of Rayleigh waves that include both a shear and axial components and that decrease exponentially in amplitude as distance from the surface increases. In this regard, they are fundamentally different from bulk shear and longitudinal acoustic waves that give rise to standard forward and backward stimulated Brillouin scattering in PCFs with lower and higher Brillouin frequency shifts, respectively. [8,10–16].

This is shown in Fig. 1(d) for the backward Brillouin spectrum that we subsequently characterized in the frequency range 8–12 GHz. As can be seen, the Brillouin spectrum involves a broadband series of frequency peaks spanning from 9 GHz to more than 11 GHz. The two small peaks at 9.12 GHz and 10.87 GHz have been identified as Brillouin backscattering from the HNA and SMF fibers present in the experimental setup. More importantly, all other frequency peaks come from the PCF and they are generated by multiple hybrid acoustic waves confined in the PCF core, as previously shown in Refs. [8,10,11]. This relies on the fact that, in such small-core PCFs, there is a strong coupling of shear and longitudinal acoustic components due to the waveguide boundaries, giving rise to multimode and broadband backward stimulated Brillouin spectra and higher power thresholds than those theoretically predicted [10]. We also note that surface acoustic resonances around 6 GHz have been numerically predicted in Ref. [10], but they have never been observed in PCFs so far. Here we report the observation of these SAWs and we will see thereafter that they are well confined at the air–silica interfaces.

Our observations were subsequently confirmed through numerical simulations using the equation of elastodynamics including the electrostriction. This equation can be written in the following form

$$\rho \frac{\partial^2 u_i}{\partial t^2} - \frac{\partial}{\partial x_j}\left(c_{ijkl} \frac{\partial u_k}{\partial x_l} \right) = \frac{\partial}{\partial x_j} \epsilon_0 \chi_{klij} [E_k E_l^*], \tag{1}$$

where ρ is the material density, u_i are the displacements, and C_{ijkl} the rank-4 tensor of elastic constants. The right-hand side

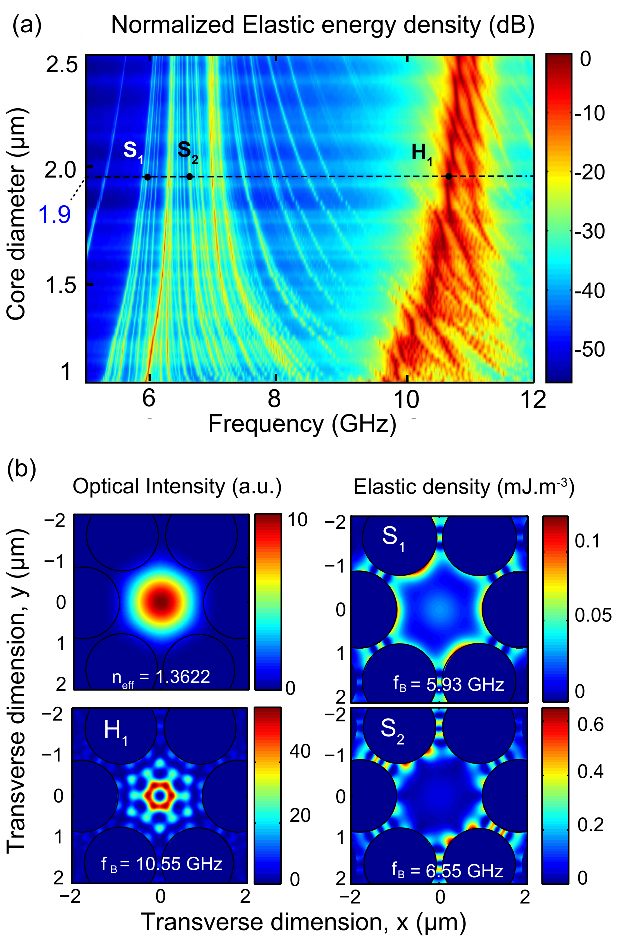

Fig. 2. Numerical simulations: (a) elastic energy density as a function of acoustic frequency and versus the PCF core diameter. (b) Poynting vector norm of the fundamental optical mode for a 1.9 µm fiber core diameter and elastic energy density of two surfaces waves S_1 at 5.93 GHz and S_2 at 6.55 GHz and one hybrid wave H_1 at 10.55 GHz labeled in (a).

of Eq. (1) is the electrostrictive stress, including the rank-4 susceptibility tensor $\chi_{klij} = \epsilon_{km}\epsilon_{ln}p_{mnij}$ with p_{mnij} the elasto-optic tensor. ϵ_0 is the permittivity of the vacuum. E_k and E_l are the pump and Brillouin Stokes fields with angular frequencies $\omega_{1,2}$ and axial wave vectors $k_{1,2}$. More details about the theoretical modelling and numerical computing method can be found in Ref. [17]. Solving numerically Eq. (1) for the backward case yields the elastic energy density and all the longitudinal and transverse displacements inside the microstructured fiber. To get better insight, we assumed a perfectly symmetric air-hole microstructure, keeping the same opto-geometric parameters as those listed in Fig. 1. We also neglected the moving boundaries effect or radiation pressure that is smaller than the electrostrictive stress due to the weak acoustic index difference between silica and air [18,19].

Figure 2(a) shows a false color rendering for the elastic energy density as a function of acoustic frequency and fiber core diameter. As shown in the simulation, we retrieve most of the observed acoustic resonances around 6 GHz and 10 GHz, all varying in frequency with the PCF core diameter according to the phase-matching. We note, however, that numerically computed spectra exhibit more acoustic branches than those experimentally observed. This is mainly due to the fact that we did not include a perfectly-matched layer (PML) for the absorption of acoustic waves around the PCF core. Nevertheless, we can readily find in Fig. 2(a) similar acoustic frequencies as those experimentally measured for two surface waves labelled S_1, S_2, and the main hybrid wave labelled H_1 [see dashed black line for a core diameter of 1.9 µm and compare to Figs. 1(c) and 1(d)]. We then plotted in Fig. 2(b) the spatial intensity distribution of the fundamental optical mode (norm of the Poynting vector of the HE_{11} mode), and the elastic energy density of these three acoustic resonances S_1, S_2, and H_1. We note that the elastic energy for S_1 and S_2 is mainly distributed near the air holes of the fiber, whereas for H_1 it is mostly confined into the core. This clearly indicates that S_1 and S_2 are related to SAWs with an elastic energy that decreases rapidly when moving away from the surface. From numerical simulations, we can also deduce the ratio of transverse displacement over the total displacement (transverse plus longitudinal displacements), which we denote as $|\frac{u_S}{u_T}|$. For the surface waves S_1 and S_2, we verified that this ratio approaches ≈1, while at 10.55 GHz the ratio $|\frac{u_S}{u_T}|$ tends towards 0.5, which also confirms the different nature of these hybrid waves.

We then performed a series of numerical simulations by varying the air-filling fraction d/Λ of the air–silica microstructure keeping the same pitch. Figure 3 shows the evolution of both the acoustic frequency of the strongest SAW and its elastic energy density versus the air-filling ratio. As can be seen, the elastic energy increases exponentially when increasing d/Λ while both the surface acoustic frequency and core diameter decrease. This is also confirmed by the two images shown in the inset of Fig. 3 that compare the transverse elastic energy for two extreme values of d/Λ. All the elastic energy is localized near the first air hole ring of the microstructure when the air-filling ratio becomes sufficiently large.

Subsequently, we experimentally showed that small-core PCFs offer a way to control Brillouin light scattering from SAWs, with the advantages of longer distance than short fiber taper and more degrees of freedom, such as the pitch and the

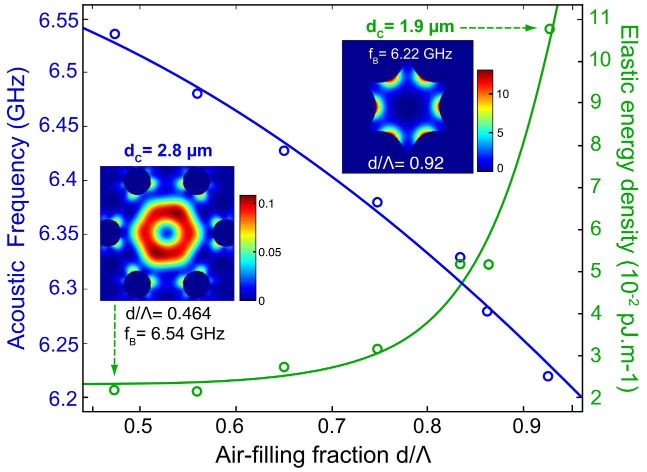

Fig. 3. Numerical simulation of the surface acoustic frequency (blue circles, left axis) and the maximum elastic energy density (green circles, right axis) as a function of the air-filling fraction of the PCF. The solid red and black lines show quadratic and exponential fits, respectively.

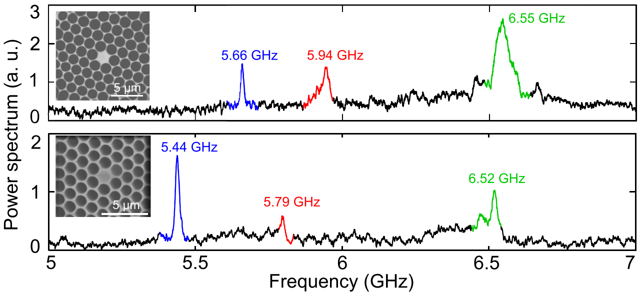

Fig. 4. Experimental Brillouin spectra measured in two different core-size photonic crystal fibers at 1.55 μm using heterodyne detection.

air-filling ratio. Figure 4 compares the experimental Brillouin spectra measured in two different core-size silica PCFs shown in the insets. The first fiber is the same as that used previously, while the second one has both a smaller core diameter ($d_c = 1.57\ \mu\text{m}$) and air-filling ratio ($d/\Lambda = 0.91$). In both cases, we can clearly see three main peaks around 6 GHz as the result of SAW-induced Brillouin scattering. A further comparison of the two spectra shows a clear rightward shift of the Brillouin peaks due to the fact that the effective refractive index decreases with the core size, while the amplitude difference mainly comes from the microstructure irregularities. These observations indicate that one can finely control the acoustic frequencies of surface Brillouin scattering by tailoring the fiber air-hole microstructure.

In summary, we demonstrated both experimentally and numerically Brillouin light scattering from multiple surface and hybrid acoustic waves in a small-core and high air-filling fraction photonic crystal fiber. We showed that these new acoustic resonances generated around 6 GHz are mainly localized near the air holes and decrease exponentially in amplitude as distance from the surface increases. While the SAWs are comparable to those previously observed in subwavelength-diameter tapered optical fibers [3], the use of small-core PCFs offers unprecedented opportunities for controlling and enhancing surface Brillouin scattering. Finally, as SAWs are inherently sensitive to surface defects and features, this new type of Brillouin scattering may prove interesting for applications to optical sensing that can exploit surface acoustic waves, or for precise measurement of surface roughness of microstructured optical fibers. For that purpose, we will in the near future characterize the temperature tuning coefficients of surface acoustic waves in photonic crystal fibers, as in Ref. [20].

Funding. Agence Nationale de la Recherche (ANR) (ANR-14-CE36-0005-01); Région de Franche-Comté; LABEX ACTION Program (ANR-11-LABX-0001-01); TOP-WAVE (ANR-13-JS04-0004); Labex CEMPI (ANR-11-LABX-0007); Equipex FLUX (ANR-11 EQPX-0017).

REFERENCES

1. P. Mutti, C. E. Bottani, G. Ghislotti, M. Beghi, G. A. D. Briggs, and J. R. Sandercock, “Surface Brillouin scattering—extending surface wave measurements to 20 GHz,” in *Advances in Acoustic Microscopy* (Springer, 1995), pp. 249–300.
2. J. D. Comins, *Handbook of Elastic Properties of Solids, Liquids, and Gases*, Vol. **I** of Dynamic Methods for Measuring the Elastic Properties of Solids (Academic, 2001).
3. J.-C. Beugnot, S. Lebrun, G. Pauliat, H. Maillotte, V. Laude, and T. Sylvestre, Nat. Commun. **5**, 5242 (2014).
4. O. Florez, P. F. Jarschel, Y. A. Espinel, C. Cordeiro, T. P. M. Alegre, G. S. Wiederhecker, and P. Dainese, Nature Commun. **7**, 11759 (2016).
5. R. N. Thurston, J. Acoust. Soc. Am. **64**, 1 (1978).
6. D. Royer and E. Dieulesaint, *Elastic Waves in Solids I: Free and Guided Propagation* (Springer, 2000).
7. G. P. Agrawal, *Nonlinear Fiber Optics* (Academic, 2007).
8. J. C. Beugnot, T. Sylvestre, D. Alasia, H. Maillotte, V. Laude, A. Monteville, L. Provino, N. Traynor, S. F. Mafang, and L. Thévenaz, Opt. Express **15**, 15517 (2007).
9. A. Kobyakov, M. Sauer, and D. Chowdhury, Adv. Opt. Photon. **2**, 1 (2010).
10. P. Dainese, P. S. J. Russell, N. Joly, J. Knight, G. Wiederhecker, H. L. Fragnito, V. Laude, and A. Khelif, Nat. Phys. **2**, 388 (2006).
11. J. C. Tchahame, J.-C. Beugnot, A. Kudlinski, and T. Sylvestre, Opt. Lett. **40**, 4281 (2015).
12. D. Elser, U. L. Andersen, A. Korn, O. Glöckl, S. Lorenz, C. Marquardt, and G. Leuchs, Phys. Rev. Lett. **97**, 133901 (2006).
13. J.-C. Beugnot, T. Sylvestre, H. Maillotte, G. Mélin, and V. Laude, Opt. Lett. **32**, 17 (2007).
14. B. Stiller, M. Delqué, J.-C. Beugnot, M. W. Lee, G. Mélin, H. Maillotte, V. Laude, and T. Sylvestre, Opt. Express **19**, 7689 (2011).
15. M. S. Kang, A. Nazarkin, A. Brenn, and P. S. J. Russell, Nat. Phys. **5**, 276 (2009).
16. A. Brenn, G. S. Wiederhecker, M. S. Kang, H. Hundertmark, N. Joly, and P. S. Russell, J. Opt. Soc. Am. B **26**, 1641 (2009).
17. J.-C. Beugnot and V. Laude, Phys. Rev. B **86**, 224304 (2012).
18. P. T. Rakich, Z. Wang, and P. Davids, Opt. Lett. **36**, 217 (2011).
19. V. Laude and J.-C. Beugnot, New J. Phys. **17**, 125003 (2015).
20. E. Carry, J.-C. Beugnot, B. Stiller, M. W. Lee, H. Maillotte, and T. Sylvestre, Appl. Opt. **50**, 6543 (2011).